Chemistry–A European Journal

Research Article
doi.org/10.1002/chem.202404432

Chemistry Europe
European Chemical
Societies Publishing

www.chemeurj.org

Supramolecular Assembly of Water-Soluble Platinum(II) Complexes: From Emission Modulation to Cell Imaging in Specific Organelles

Tobias Rex,[a, b] Theresa Mößer,[c] Raquel R. C. Vilela,[d] Alexander Hepp,[a] Carsten Grashoff,[c] and Cristian A. Strassert*[a, b]

The control of self-organized metal complexes presents advantages regarding the modulation of luminescence through dynamic assembly, rendering them promising for bioimaging. Herein, we demonstrate a strategy towards a series of amphiphilic Pt(II) complexes featuring bis-cyclometalated ligands as tetradentate luminophores, which exhibit enhanced water solubility and tuneable self-assembly properties. The resulting nanostructures can be precisely controlled by adjusting concentration and solvent composition, yielding switchable luminescence from red (i.e., excimer-based) to green (i.e., monomer-centred) and reversible (dis−)assembly of the aggregates. Cytotoxicity assays confirmed the innocuous nature of

these luminophores at concentrations below 10 µM, while cellular uptake studies demonstrated effective internalization in both living and fixed cells. Using photoluminescence lifetime imaging micro(spectro)scopy, we determined that the complexes localized preferentially within lysosomes of living cells, while accumulating in the nuclei of fixed cells, with differences in photophysical behavior depending on whether the species were monomeric or excimeric in nature. These new findings provide insights into the systematic design of water-soluble Pt(II)-based luminophores with photophysical properties controlled by supramolecular interactions, underlining their potential for use in cellular imaging and diagnostics.

Introduction

Supramolecular chemistry offers a powerful approach for constructing large molecular architectures through noncovalent interactions, distinguishing it from traditional macromolecular chemistry, which primarily relies on covalent or coordinative bonds for structural formation.[1] Among the various strategies in supramolecular chemistry, the use of amphiphilic molecules stands out as an effective technique for the design of self-assembling systems.[2] Molecular entities containing both hydrophilic and hydrophobic domains possess the unique ability to spontaneously organize into well-defined molecular nanostructures, such as micelles and vesicles, particularly when placed in

aqueous environments.[3] This self-organization process results in nanostructures with distinct physical and chemical properties compared to their monomeric counterparts.[4] The exploitation of this behavior has significantly increased interest in supramolecular chemistry in recent decades, demonstrating its potential for applications in diverse fields ranging from materials science to biomedicine.[5]

The assembly of nanostructures from transition metal complexes (TMCs) is a growing research area, offering new opportunities to develop functional materials with distinctive features.[6] Platinum(II) complexes have proven particularly versatile in this context, due to their outstanding photophysical properties and easily tunable ligand design. The square-planar coordination geometry, combined with π-conjugated ligands, tends to promote sizeable metal-metal and/or π-π-stacking interactions, positioning such complexes as ideal candidates for new classes of supramolecular materials.[7,8] Besides, when the Pt atoms come into close proximity (around 3.5 Å or less, typically supported through *van der Waals* interactions), both excitation and emission energies can be shifted towards the red part of the electromagnetic spectrum, if compared with the monomeric species. This shift is attributed to the accessibility of excited metal-metal-to-ligands charge-transfer (^{3}MMLCT) triplet states with variable degrees of ground state coupling or excimeric character, as opposed to the metal-perturbed ligand-centered (^{3}MP-LC) nature of the non-interacting monomers.[9,10] Hence, while randomly oriented molecular arrangements within aggregates lead to intermolecular quenching, face-to-face dimerization enables metal-metal contacts with variable degrees of ground state coupling or excimer character (in the latter, the interaction is stronger in the excited state). In this

[a] T. Rex, A. Hepp, C. A. Strassert
Institut für Anorganische und Analytische Chemie, Universität Münster,
Corrensstraße 28–30, D-48149 Münster, Germany
E-mail: ca.s@wwu.de

[b] T. Rex, C. A. Strassert
CeNTech, Universität Münster, Heisenbergstraße 11, D-48149Münster,
Germany

[c] T. Mößer, C. Grashoff
Institute of Integrative Cell Biology and Physiology, Universität Münster,
Schlossplatz 5, D-48149, Münster, Germany

[d] R. R. C. Vilela
São Carlos Institute of Physics, University of São Paulo,13566-590, São
Carlos, Brazil

Chemistry–A European Journal

Research Article
doi.org/10.1002/chem.202404432

Chemistry Europe
European Chemical
Societies Publishing

context, the use of tetradentate bis-cyclometallated lumino-phores has attracted considerable attention due to their improved properties. Compared to bidentate or tridentate chelators, their highly rigid coordination environment significantly improves the photophysical properties by effectively reducing the non-radiative deactivation constant. In addition, tetradentate ligands are characterized by their high kinetic and thermodynamic stability, which avoids the detachment of auxiliary ligands and ensures structural robustness.[7,11]

Incorporating Pt(II) centers into amphiphilic molecular architectures takes advantage of these features, enabling modulation of photophysical and photochemical properties through the dynamic interplay of different emissive states. This approach has led to the self-organization of Pt(II) complexes into a variety of nanostructures such as nanosheets,[12] nanotubes,[13] nanofibers[14] and liquid crystals.[15,16] These assemblies have been widely investigated for applications including catalysis, optical sensors and luminescent devices.[17]

Beyond materials science, Pt(II) complexes have emerged as potent tools in biomedicine, particularly for bioimaging applications. Notably, for some amphiphilic Pt(II) complexes, the self-assembly into well-ordered nanostructures can result in enhanced photoluminescence quantum yields (PLQY, $i.e.$, Φ_L) and a broader range of emission colors compared to their non-assembled monomeric forms.[8,9] Furthermore, Pt(II) complexes are known for their relatively long excited triplet state lifetimes (τ) and significant Stokes shifts related to their phosphorescent nature, which can be helpful to eliminate background auto-fluorescence from biological tissues towards an enhanced contrast.[18] These properties are crucial for developing luminescent probes with high sensitivity and selectivity, especially in biological microenvironments where low signal-to-noise ratios often limit imaging techniques. In particular, their relatively long radiative deactivation kinetics allows the use of time-resolved or time-gated detection techniques to yield lifetime maps. Hence, since luminescent species require a certain degree of hydrophobicity to cross the phospholipidic cell membrane and be internalized, amphiphilic complexes are particularly advantageous. Therefore, creating Pt(II) complexes with a tendency to form supramolecular structures mimicking biological self-organization represents an interesting approach for advances in bioimaging supported by increased cellular uptake with enhanced signal-to-noise ratio accompanied by the improvement of compartment-specific accumulation. However, despite these advantages, several challenges remain in the implementation of platinum complexes: Issues including excitation wavelengths in the ultraviolet region with low molar absorption coefficients as well as poor water solubility can hinder their performance in biological environments. These problems highlight the importance of ligand design in overcoming these limitations and expand the applicability of Pt(II) complexes both in fundamental studies and in biomedical contexts.

Herein, we report the design and synthesis of three novel amphiphilic dianionic Pt(II)-based coordination compounds bearing tetradentate luminophores that act as bis-cyclometalated ligands with significantly improved water solubility. We examined the formation of supramolecular nanostructures and demonstrated the ability to control the emission colors by adjusting the concentrations in water and the solvent composition (water/methanol mixtures). Hence, variation of the hydrophilic moieties through differently charged groups led to different self-assembly behaviors, going from purely monomeric species to sizeable aggregation at concentrations below 10 µM. A combination of size and morphological analyses allowed the structural characterization of the resulting nano-aggregates. Additionally, we evaluated the cytotoxicity and the cellular uptake in living and fixed cells while analyzing the localization in subcellular compartments and organelles with the aid of photoluminescence lifetime imaging micro(spectro)scopy (PLIM). This allowed us to determine whether the monomeric or aggregated species with or without excimer character were predominant under physiological conditions, providing insights into their behavior in a cellular microenvironment.

Results and Discussion

Molecular Design

In order to develop self-assembling Pt(II) complexes with tetradentate luminophores providing a square-planar coordination environment, a series of three complexes with amphiphilic nature were designed. Thus, the simultaneous presence of a hydrophobic alkyl chain and variably hydrophilic end-groups would facilitate self-assembly and disassembly under particular conditions. The synthesis route towards the three complexes is depicted in Scheme 1 and is based on the improved methodology previously established and optimized in our group.[16,19]

The three complexes have distinct hydrophilic moieties, particularly sulfonate (**Pt-SO₃K**), carboxylate (**Pt-CO₂K**) or spermine (**Pt-Sperm**) units. This variation is intended to promote the development of differently self-assembled structures by modulating the charge of the complex. The synthesis is divided into two main pathways, starting both with compound **2**, which was prepared in two steps according to previous work of our group for analogous C^N*N^C species (for further details, see Supporting Information - SI).[16] The two ligand precursors were obtained by a Suzuki-Miyaura cross-coupling of **2** with 4-hydroxyphenylboronic acid to provide **3** and with 4-carboxyl-phenylboronic acid to yield **5**. These ligand precursors were further implemented in a well-established double cyclometalla-tion reaction with K₂[PtCl₄] rendering the two coordination-chemical precursors **4** and **6**. **Pt-SO₃K** was finally prepared by an N-alkylation of **4** with 1,3-propane sultone in the presence of a base, whereas **Pt-CO₂K** was obtained by a Williamson's ether synthesis of **4** employing tert-butyl 2-bromoacetate followed by subsequent tert-butyl cleavage with trifluoracetic acid and base-supported deprotonation. The polyamine-decorated complex, namely **Pt-Sperm**, was obtained by the coupling of the two carboxylic acid functions from **6** with N^1,N^4,N^9-tri-boc-spermine **7** via amide bond formation, followed by removal the protecting groups with trifluoracetic acid. The three final amphiphiles were purified by medium-pressure liquid chroma-
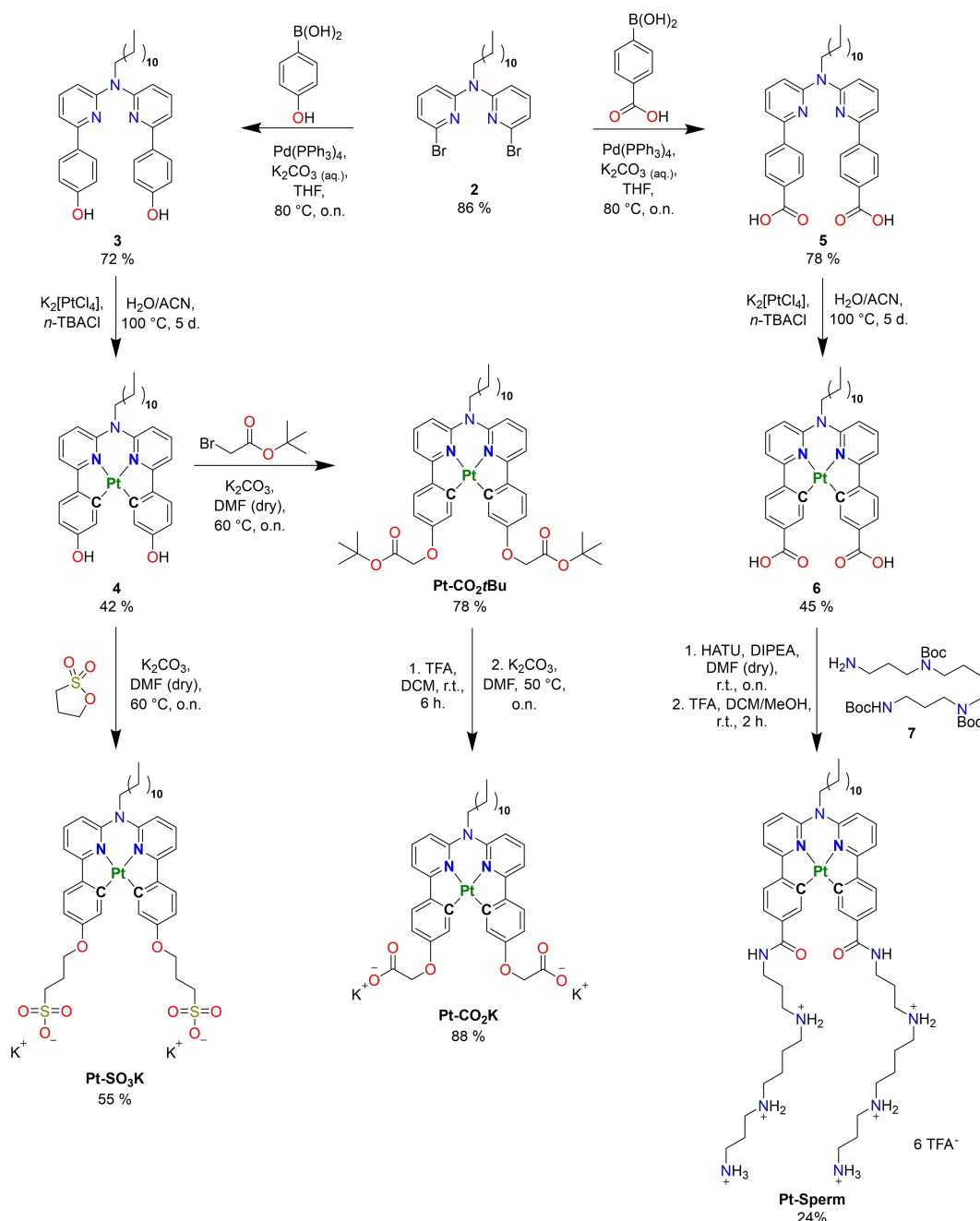
Scheme 1. Synthetic route towards the three target complexes, namely **Pt-SO₃K**, **Pt-CO₂K** and **Pt-Sperm**.

tography (MPLC), due to their conveniently high hydrophilicity. All synthetic intermediates, ligand precursors and complexes were characterized by means of 2D-NMR spectroscopy and exact mass spectrometry, where all the signals were unambiguously assigned.

UV-Vis Absorption and Photoluminescence Spectroscopic Studies

Supramolecular architectures such as micelles exhibit a dynamic behavior,[20] with monomers and assembled structures in constant equilibrium. This inherent balance between monomeric and aggregated states is reflected in the optical readouts. Therefore, the photophysical properties of the complexes **Pt-SO₃K**, **Pt-CO₂K** and **Pt-Sperm** were comparatively investigated in air-equilibrated and argon-purged solutions in water (H_2O) as well as in methanol (MeOH) (see Table 1 and Table S1) at various concentrations (10^{-6} M → 10^{-3} M) to study their tendency towards assembly into nanoaggregates.

The absorption and photoluminescence spectra are shown in Figure 1a/b. The bands between 240–350 nm are attributed to spin-allowed transitions into $^1\pi\text{-}\pi^*$ configurations, indicative of ligand-centered electronic excited states (^{1}LC). The lower

Chemistry–A European Journal

Research Article
doi.org/10.1002/chem.202404432

Chemistry
Europe
European Chemical
Societies Publishing

Table 1. Summary of photophysical data for **Pt-SO₃K**, **Pt-CO₂K** and **Pt-Sperm** in H_2O and MeOH solutions ($c \approx 10^{-5}$ M), at room temperature.

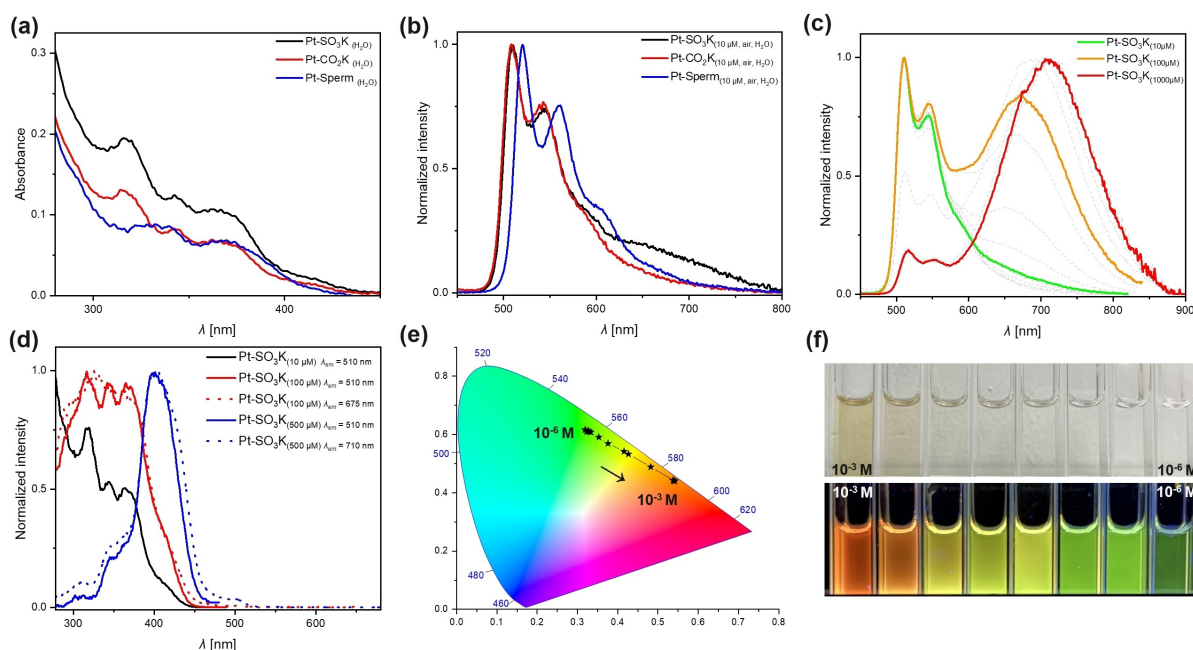|	solvent	λ_{em} (nm)	$\Phi_{L\,(air)}$ (%)	$\Phi_{L\,(Ar)}$ (%)	$\tau_{(air)}$ (ns)	$\tau_{(Ar)}$ (μs)	$k_{r\,(Ar)}$ (10⁴ s⁻¹)	$k_{nr\,(Ar)}$ (10⁴ s⁻¹)
Pt-SO₃K	H_2O	510, 545	3 ± 2	6 ± 2	669 ± 1	21.05 ± 0.03	0.3 ± 0.1	4.5 ± 0.1
	MeOH	515, 549	< 2	54 ± 3	88.9 ± 0.1	16.55 ± 0.02	3.3 ± 0.1	2.8 ± 0.1
Pt-CO₂K	H_2O	508, 543	2 ± 2	10 ± 2	721 ± 1	23.91 ± 0.04	0.4 ± 0.1	3.8 ± 0.1
	MeOH	515, 549	< 2	55 ± 3	94.8 ± 0.1	15.84 ± 0.02	3.5 ± 0.1	2.8 ± 0.1
Pt-Sperm	H_2O	520, 560	3 ± 2	9 ± 2	1361 ± 1	7.93 ± 0.01	1.1 ± 0.3	11.5 ± 0.3
	MeOH	524, 564	< 2	8 ± 2	249.2 ± 0.2	5.240 ± 0.01	1.5 ± 0.4	17.5 ± 0.4

Figure 1. UV-vis absorption spectra (a) and normalized photoluminescence emission spectra (b) of **Pt-SO₃K** (black), **Pt-CO₂K** (red) and **Pt-Sperm** (blue) in air-equilibrated H_2O solutions ($c \approx 10^{-5}$ M). (c) Photoluminescence emission spectra of **Pt-SO₃K** within the concentration range from 10^{-6} to 10^{-3} M in air-equilibrated H_2O solution. (d) Normalized photoluminescence excitation spectra of **Pt-SO₃K** monitored at different emission maxima for different concentrations. (e) Color diagram with the respective CIE coordinates for **Pt-SO₃K** in H_2O solutions at different concentrations. (f) Photographs of **Pt-SO₃K** under visible light (top) and UV light ($\lambda = 365$ nm, bottom) in H_2O solutions at different concentrations (10^{-3} M →10^{-6} M) showing the optical changes. All the measurements were performed at room temperature.

energy bands between 350–450 nm are associated to transitions into mixed ¹LC states with admixtures of metal-to-ligand charge-transfer (MLCT) character, where the contribution of the metal-centered orbitals become more prominent (Figure 1a). **Pt-SO₃K** and **Pt-CO₂K** show comparable absorption profiles, while **Pt-Sperm** does not present the characteristic band at 320 nm, reflecting the electronic differences between the cyclometalated units.

The photoluminescence spectra of **Pt-SO₃K**, **Pt-CO₂K** and **Pt-Sperm** in H_2O at lower concentrations (10 μM) exhibit emission maxima peaking between 510–520 nm, accompanied by vibrational shoulders between 543–560 nm, thus representing the monomeric state (*i.e.*, with ³MP-LC character, see Figure 1b). Notably, **Pt-Sperm** is slightly red-shifted by around 10–15 nm and shows approximately a twice as long lifetime (~1360 ns) in H_2O compared to **Pt-SO₃K** and **Pt-CO₂K** (~670 and 720 ns, respectively). Upon exclusion of oxygen, the lifetimes rise above

20 μs for **Pt-SO₃K** and **Pt-CO₂K**, and up to 8 μs for **Pt-Sperm** (Table 1). Interestingly, even at low concentrations, **Pt-SO₃K** displays a detectable red-shifted shoulder around 650 nm, pointing towards ³MMLCT-based transitions involving sizeable Pt···Pt interactions. As the concentrations increase, both **Pt-SO₃K** (Figure 1c) and **Pt-CO₂K** (see Figure S74) exhibit a gradual red shift in the emission maxima, ranging from 632 to 715 nm. This shift is characteristic for ³MMLCT states, indicating the formation of aggregated structures with shortened Pt···Pt distances and excimeric character.

The relative intensity and the energy of the emission maxima vary with the concentration for both complexes while the monomer intensity decreases due to aggregation, as can be observed by naked eye (Figure 1f and Figure S82a). The CIE plot for **Pt-SO₃K** (Figure 1e) indicates the migration of the global emission from green to red, with **Pt-SO₃K** demonstrating a higher tendency towards aggregation andexcimer formation if

Chemistry–A European Journal

Research Article
doi.org/10.1002/chem.202404432

Chemistry Europe
European Chemical
Societies Publishing

compared to **Pt-CO$_2$K** (see Figure S74). The self-assembly was further revealed by the excitation spectra and time-resolved photoluminescence decays at different concentrations in H$_2$O (10 μM, 100 μM, 500 μM, see Figure S72 and Table S1). Notably, the luminescence lifetimes of the excimeric species are shorter than those of the monomeric species for both **Pt-SO$_3$K** and **Pt-CO$_2$K** complexes, and the excitation spectra reveal an enhanced band above 450 nm (Figure 1d), indicating the different origins of the monomer and aggregate emission while pointing to intermolecular coupling in the ground state. In addition, the photoluminescence decays shift from monoexponential to multiexponential profiles (see Table S1). In general, the excited state lifetimes monitored at the emission wavelength of the monomers shorten at higher concentrations (Table S1).

Surprisingly, **Pt-Sperm** does not show any observable excimer emission with increasing concentrations (see Figure S72f). This suggests that the positively charged spermine chains may prevent electronic coupling between excited monomers. The distinct absorption profile and the emission spectrum of **Pt-Sperm** can be attributed to a different contribution of the amide groups to the highest occupied molecular orbital (HOMO), compared to the alkoxy groups in **Pt-SO$_3$K** and **Pt-CO$_2$K**. The latter can destabilize the HOMO, leading to a reduced gap between the excited and ground state (as previously observed for other Ir(III) and Pt(II) complexes).[21] The absence of excimer emission leads to invariant photoluminescence lifetimes for **Pt-Sperm** at all concentrations (see Table S1). Furthermore, **Pt-Sperm** exhibits relatively lower photoluminescence quantum yields (Table 1), which could be due to photoinduced electron transfer leading to quenching of excited species by the polyamine chains while preventing the formation of excimers, thus altering the local microenvironment and leading to distinct photophysical properties. These findings suggest that differences in the substitution pattern significantly affect the self-assembly equilibria, with only the negatively charged units promoting excimer emission at higher concentrations through the combination of Pt···Pt and π-π stacking

interactions in H$_2$O. In general, the complexes demonstrate an outstanding H$_2$O solubility and sizeable phosphorescence even at higher concentrations.

To monitor the self-aggregation process, the ratio of the red emission intensity (associated with excimeric ^{3}MMLCT character, I_{red}) to the green emission intensity (originating from the monomeric ^{3}MP-LC state, I_{green}) was employed to determine the critical micellar concentration (CMC). This ratio provides insight into the onset of self-aggregation, where an increase in I_{red} relative to I_{green} indicates the formation of micelles. Figure S83 illustrates the variation of the I_{red}/I_{green} ratio as a function of concentration. At lower concentrations, the I_{red}/I_{green} ratio remains low, with the emission dominated by the ^{3}MP-LC character. As the concentration increases, micelle formation intensifies, leading to a pronounced increase in the I_{red}/I_{green} ratio. The CMC can then be determined by the intercept of two straight lines. This approach provides a sensitive method for tracking the aggregation process of Pt(II) complexes in solution. The I_{red}/I_{green} ratio was measured across various concentrations of **Pt-SO$_3$K** and **Pt-CO$_2$K**, with the CMC values determined to be 47 μM and 215 μM, respectively.

The tendency to self-assemble in solution was further investigated *via* a solvent change from water to a polar organic solvent (MeOH) while analyzing mixtures of H$_2$O/MeOH. In MeOH, for all three complexes only the monomer-based emission is observed, even at higher concentrations (Figure 2a and Figure S75). Comparing the photophysical properties in MeOH and H$_2$O, three observations stand out: First, all complexes reveal a red-shifted monomer emission in MeOH; second, the relaxation to the ground state of the monomeric species of all three complexes is slower in H$_2$O than in MeOH for both air-equilibrated and Ar-purged solutions; third, the quantum yields in Ar-purged MeOH is drastically increased for **Pt-SO$_3$K** and **Pt-CO$_2$K** (Table 1).

The significant increase in the radiative (k_r) and the decrease in non-radiative deactivation rates (k_{nr}) observed for **Pt-SO$_3$K** and **Pt-CO$_2$K** in Ar-purged MeOH compared to Ar-purged H$_2$O
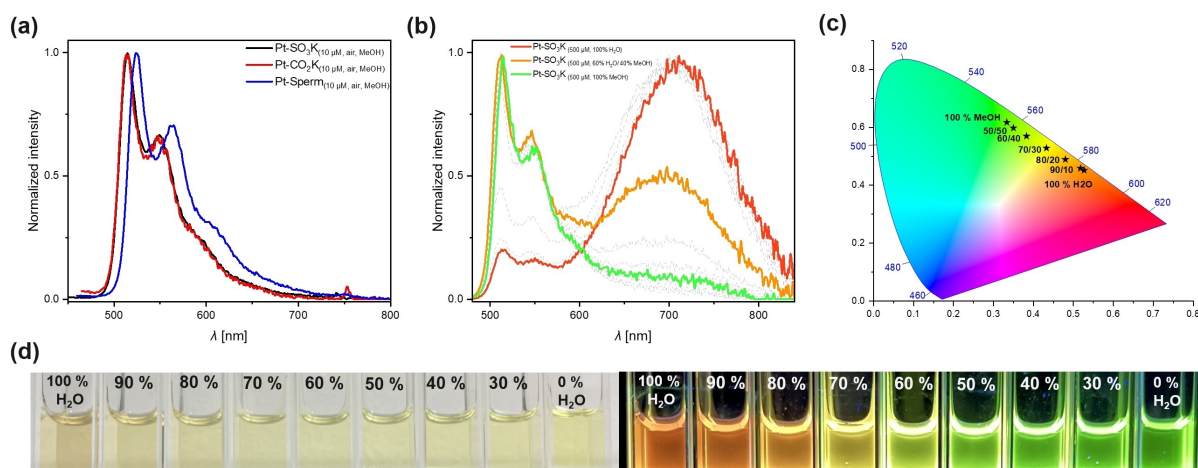

Figure 2. (a) Normalized photoluminescence emission spectra of **Pt-SO$_3$K** (black), **Pt-CO$_2$K** (red) and **Pt-Sperm** (blue) in air-equilibrated MeOH solution ($c \approx 10^{-5}$ M). (b) Normalized photoluminescence emission spectra of **Pt-SO$_3$K** for different solvent compositions (H$_2$O/MeOH) at 500 μM and (c) color diagram with the corresponding CIE coordinates. (d) Photographs of **Pt-SO$_3$K** under visible light (left) and irradiation ($\lambda = 365$ nm, right) with increasing MeOH content in H$_2$O. All the measurements were performed at room temperature.

Chemistry–A European Journal

Research Article
doi.org/10.1002/chem.202404432

Chemistry Europe
European Chemical
Societies Publishing

suggest that these complexes form non-defined molecular clusters as they begin to aggregate in H_2O, yet without an observable red shift in the emission spectra (*i.e.*, no defined excimer formation), even at low concentrations. This self-assembly effectively shields the complexes from oxygen quenching, leading also to an increased Φ_L in air-equilibrated H_2O compared to air-equilibrated MeOH. In contrast, the complexes are fully solvated in MeOH, which enhances the ^{1}MLCT character and finally results in the increase of k_r (as the metal perturbation rises and favours the phosphorescent deactivation). **Pt-Sperm**, however, does not exhibit this trend of k_r in Ar-purged solvents. Instead, an increase of k_{nr} is observed in MeOH, which can be attributed to the quenching influence of the polyamines and counterions. Notably, the excited state lifetimes of **Pt-Sperm** are practically independent of the concentration, both in MeOH and H_2O, pointing to the absence of intermolecular quenching phenomena (Table S1).

Interestingly, the self-assembled nanostructures of **Pt-SO$_3$K** and **Pt-CO$_2$K** completely disassemble in water at lower concentrations (10 μM and 100 μM) upon addition of MeOH reaching a 30% content (while leading to a drastic shift in the luminescence color as the red emission bands disappear for both complexes, see Figures S76, S77, S79 and S80; nonetheless, in pure MeOH, the excited state lifetimes become shorter at higher concentrations, pointing to intermolecular quenching, as seen in Table S1). As the MeOH content in the solvent mixture gradually increases, the phosphorescence shifts from red to yellow and eventually to green (Figure 2d and Figure S82b). This effect is attributed to the increased solvation of the hydrophobic C$_{12}$-chains at higher MeOH content, resulting in the breakdown of molecular aggregates into monomeric species. At higher concentrations, around 500 μM, the tendency of **Pt-SO$_3$K** and **Pt-CO$_2$K** to self-assemble becomes so dominant that a content of 60% MeOH is required to fully break-up the aggregates, allowing for fine-tuned control over the green-to-red emission ratio (Figure 2b/c and Figure S81). These findings highlight the crucial role of solvent polarity in modulating the self-assembly and photophysical properties of **Pt-SO$_3$K** and **Pt-CO$_2$K**, providing a versatile strategy to control their emission properties in solution.

Self-Assembly Study

To gain a deeper understanding of both the properties and morphologies of the self-assembled Pt(II) complexes in aqueous solutions, dynamic light scattering (DLS), zeta potentials (ζ-potential) and scanning electron microscopy (SEM) measurements were performed at variable concentrations (10 μM, 100 μM and 500 μM). The DLS analysis revealed that **Pt-SO$_3$K** and **Pt-CO$_2$K** already form aggregates at 10 μM with an average diameter of 135 nm for **Pt-SO$_3$K** and of 146 nm for **Pt-CO$_2$K**, indicating incipient stages of self-assembly (see Table S2 and Figure S128). Aggregation with concomitant excimer formation increases as the concentration of both complexes rises, which is consistent with the red-shifted emission observed in the photophysical studies and is therefore attributed to the increased

formation of nanostructures. Interestingly, the size of self-assembled architectures for **Pt-SO$_3$K** and **Pt-CO$_2$K** stabilizes around 200 nm, indicating the formation of ordered and stable structures. Once a certain concentration has been reached, multiple noncovalent interactions (including Pt···Pt contacts as well as π-π and electrostatic interactions) equilibrate to stabilize the self-organized assemblies. The ζ-potential further supports these findings, revealing a pronounced negative charge for the self-assembled micelles (Table S2 and Figure S129). This indicates that the sulfonate and carboxylate groups are primarily located on the micelles' outer surface, contributing to their hydrophilic character.

The SEM images complement the DLS and ζ-potential measurements, by providing visual confirmation of the self-assembled structures. Micelle-like spheres were observed for both **Pt-SO$_3$K** and **Pt-CO$_2$K** compounds at 10 μM, 100 μM and 500 μM (Figure 3). The diameters are in the range of 200-300 nm, which is consistent with the results from DLS measurements. At 500 μM, larger structures were occasionally found, likely due to the collapse micelles during samples preparation, as DLS did not reveal the formation of larger structures at this concentration. In contrast, despite a measured particle formation of **Pt-Sperm** by DLS (with a diameter of the order of 100 nm), no distinct structures were visible in the SEM images (see Figure S130). This is coherent with the photophysical patterns previously observed at different concentrations (*vide supra*). Notably, the ζ-potential for **Pt-Sperm** was found to be highly positive, with a value of +97 mV at 500 μM, which can be attributed to the presence of its positively charged polyamine chain. The combined DLS and SEM analysis clearly demonstrates that **Pt-SO$_3$K** and **Pt-CO$_2$K** yield stable nanospheres in aqueous solutions, with consistent sizes across multiple concentrations. Furthermore, the increase in aggregate size and quantity correlates with the observed red shifts in their emission profiles, reinforcing the relationship between self-assembly and photophysical properties.

Cell Imaging and Cytotoxicity

In view of the different behavior between the self-assembly of micelles and stable monomers, as well as the varying charges of the water-soluble complexes **Pt-SO$_3$K**, **Pt-CO$_2$K** and **Pt-Sperm**, their potential for distinct subcellular localizations were examined in both live and fixed cells.

Fibroblast cells were incubated with 10 μM of **Pt-SO$_3$K**, **Pt-CO$_2$K** and **Pt-Sperm** for 1 h or 24 h and visualized on a confocal microscope. At this concentration the molecules are expected to behave as monomeric species in the cell culture medium; indeed, no visible excimer formation was noted. However, after incubating living cells for 1 h and 24 h, we observed an intense green luminescence within the cells (Figure 4, $\lambda_{ex} = 405$ nm), which was not observed in untreated control cells (Figure S134), indicating a successful uptake of the three complexes. To examine the subcellular localization of the complexes, co-localization studies were performed after culturing the live fibroblasts with **Pt-SO$_3$K**, **Pt-CO$_2$K** and **Pt-Sperm**. As shown in
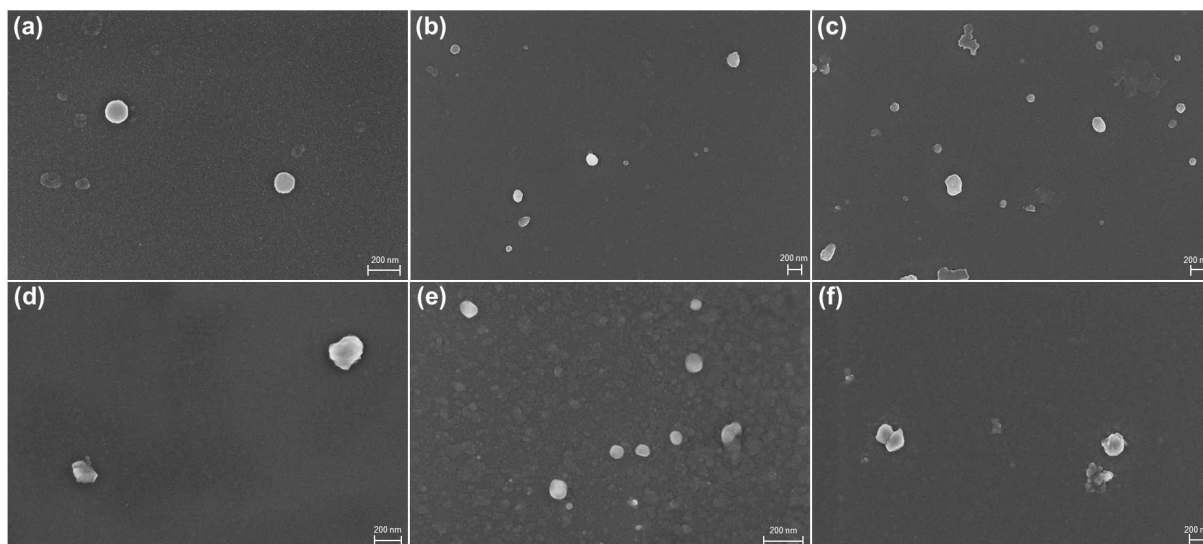
Figure 3. SEM images of **Pt-SO$_3$K** at different concentrations: a) $c \approx 10$ μM, b) $c \approx 100$ μM and c) $c \approx 500$ μM in H$_2$O. SEM images of **Pt-CO$_2$K** at different concentrations: d) $c \approx 10$ μM, e) $c \approx 100$ μM and f) $c \approx 500$ μM in H$_2$O.
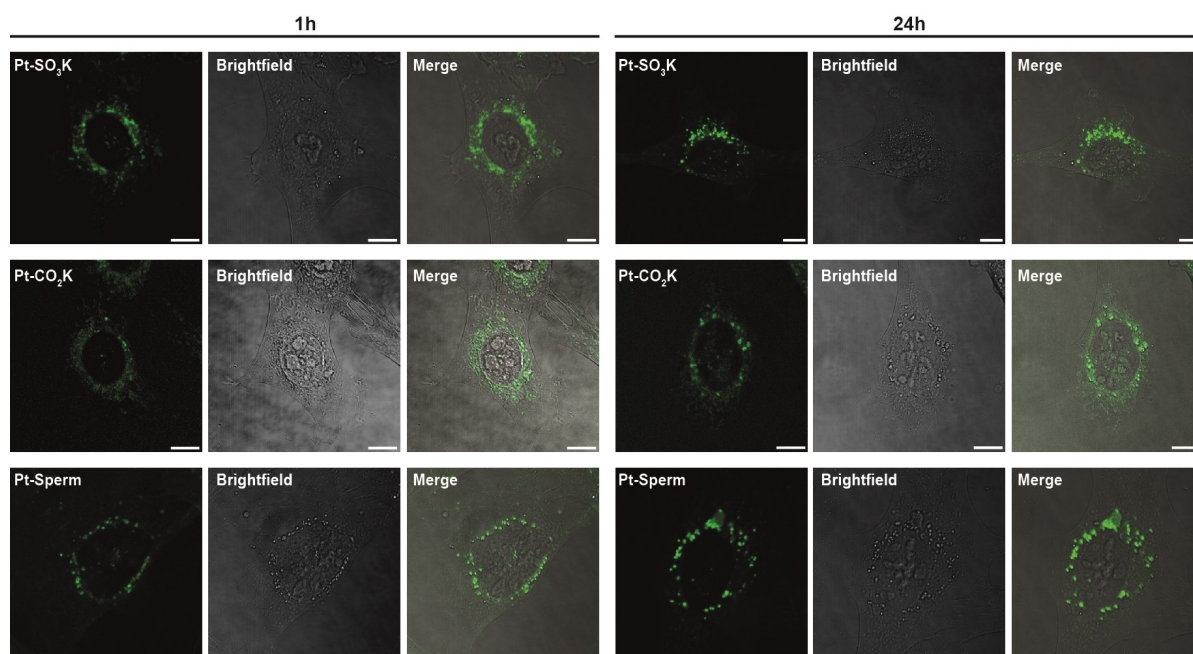
Figure 4. Confocal luminescence images ($\lambda_{ex} = 405$ nm; $\lambda_{em} = 481$–570 nm), bright field images and their overlay of living fibroblasts incubated with 10 μM **Pt-SO$_3$K**, **Pt-CO$_2$K** and **Pt-Sperm** in culture medium for 1 h and 24 h at 37 °C. The image was processed with the express deconvolution feature of Huygens Professional software. Scale bar 10 μm.

Figure 5, the green emission signal of all three complexes seemingly overlapped with the lysosomal marker LysoTracker™ Deep Red, and Pearson's and Manders' correlation coefficients indeed underlined a specific accumulation of the complexes in lysosomes (Figure S133).

Next, we tested the cytotoxicity of the three complexes in fibroblasts by treating cells with three different concentrations (1 μM, 10 μM and 100 μM) for 1 h and 24 h and subjecting cells to an MTT assay, which measures the metabolic activity of cells (Figure 6). The results suggest that all three complexes possess a relatively low toxicity at 1 μM, whereas increasing the concentration to 10 μM and 100 μM leads to a gradual decrease in cell viability for **Pt-SO$_3$K** and **Pt-Sperm**. Of note, cell viability after 24 h of incubation seemed even slightly increased, which we attribute to different cell densities used in both assays with higher cell numbers after 24 h. In general, the cytotoxic effect of **Pt-Sperm** can be attributed to the polyamine chains, in particular spermine, which is known for exhibiting cytotoxicity at high concentrations. The IC$_{50}$ value for complex **Pt-Sperm** ranges from 10 to 17 μM (after 1 h and 24 h); this range is
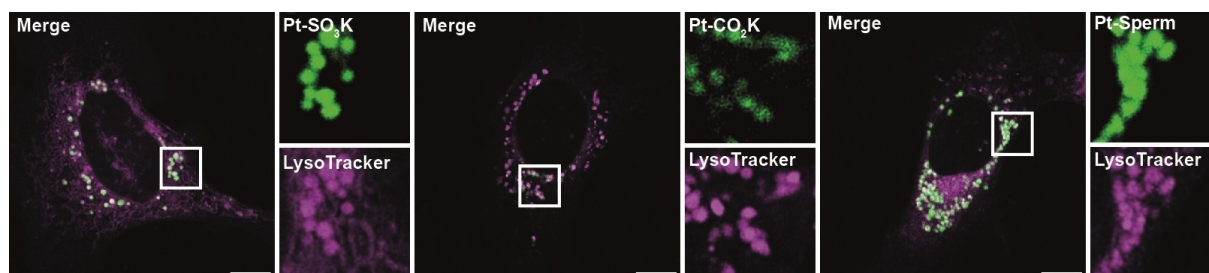
Chemistry–A European Journal

Research Article
doi.org/10.1002/chem.202404432

Chemistry Europe
European Chemical
Societies Publishing

Figure 5. Colocalization studies in living fibroblasts incubated with **Pt-SO₃K**, **Pt-CO₂K** and **Pt-Sperm** at 10 μM (λ_{ex} = 405 nm; λ_{em} = 481–570 nm) and LysoTracker™ Deep Red (λ_{ex} = 633 nm; λ_{em} = 651–686 nm) indicate accumulation of the complexes in lysosomes. Small images present an enlarged view of the selected areas highlighted by white boxes. The image was processed with the express deconvolution feature of Huygens Professional software. Scale bar 10 μm.
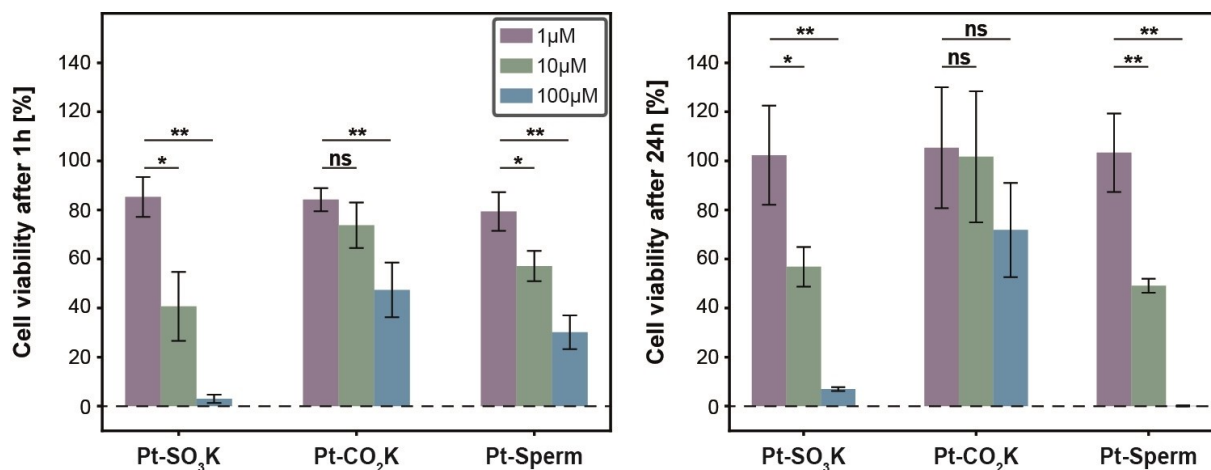
Figure 6. Viability of cells after incubation with **Pt-SO₃K**, **Pt-CO₂K** and **Pt-Sperm** for 1 h (left) and 24 h (right). Cells were treated with three different concentrations per complex: 1 μM, 10 μM and 100 μM and data show the mean viability values normalized to untreated controls ± SD (n = 3). Statistical differences were determined with a paired t-test. *P < 0.05; **P < 0.01; ns, P ≥ 0.05.

consistent with IC_{50} values observed for other spermine derivatives.[22] In addition, it is known that structural modifications involving sulfonate groups enhance the cytotoxicity, which may explain the pronounced cytotoxic effect of **Pt-SO₃K**;[23] thus, cells cultured with **Pt-CO₂K** showed the least impact on cell viability. Importantly, concentrations of 10 μM did not induced notable cell death in the here tested cells as would be indicated by loss of cell adhesion and cell detachment. We infer from these observations that the lowered metabolic activity at 10 μM is primarily caused by a reduced proliferation rate after the addition of the Pt-complexes.

To explore whether increased incubation times lead to a higher accumulation accompanied by an aggregation and emission red shift, we performed live cell imaging monitoring two emission wavelength channels (green 481 - 570 nm *vs.* red channel 590 - 680 nm). To obtain sufficiently high signal intensities and allow a direct comparison with the data above (Figures 4 and 5), we incubated cells with Pt-complex concentrations of 10 μM. These experiments revealed that a luminescence signal can be observed in both channels (see Figure S131). To explore if the noticed emission originated from monomeric or excimeric structures, we analyzed the green-to-red ratio of the two channels after 1 h *vs.* 24 h. After 24 h, a

higher accumulation was observed by an intensity increase for **Pt-SO₃K** and **Pt-Sperm** (Figure 7a). In contrast, **Pt-CO₂K** showed minimal luminescence, the intensity of which did not increase significantly with prolonged incubation, suggesting a lower cellular uptake of this complex. Our analysis revealed that the green-to-red ratio of **Pt-SO₃K** and **Pt-Sperm** remained constant with higher accumulation in the living cell, indicating that the monomeric species is predominant in the cellular environment (*i.e.*, it behaves as the monomeric species in MeOH). Consequently, the signal detected in the red channel is exclusively due to the tail of the monomeric emission in the red spectral region.

To further confirm this observation, the excited state lifetimes of the complexes in the cells were determined using photoluminescence lifetime imaging micro(spectro)scopy (PLIM). Due to the weak emission intensity and low accumulation of **Pt-CO₂K**, PLIM measurements were not feasible for this complex. However, the lifetimes of **Pt-SO₃K** and **Pt-Sperm** monomers increased (**Pt-SO₃K**: $\tau_{av\_amp/16\ cells}$ = 1330 ± 60 ns; **Pt-Sperm**: $\tau_{av\_amp/16\ cells}$ = 1960 ± 170 ns; Figure 7b and Figure S135, S136, Table S3) compared to the monomeric lifetimes in H_2O solution (**Pt-SO₃K**: τ = 669 ± 1 ns; **Pt-Sperm**: τ = 1361 ± 1 ns; Table 1). This enhancement in lifetimes is attributed to micro-
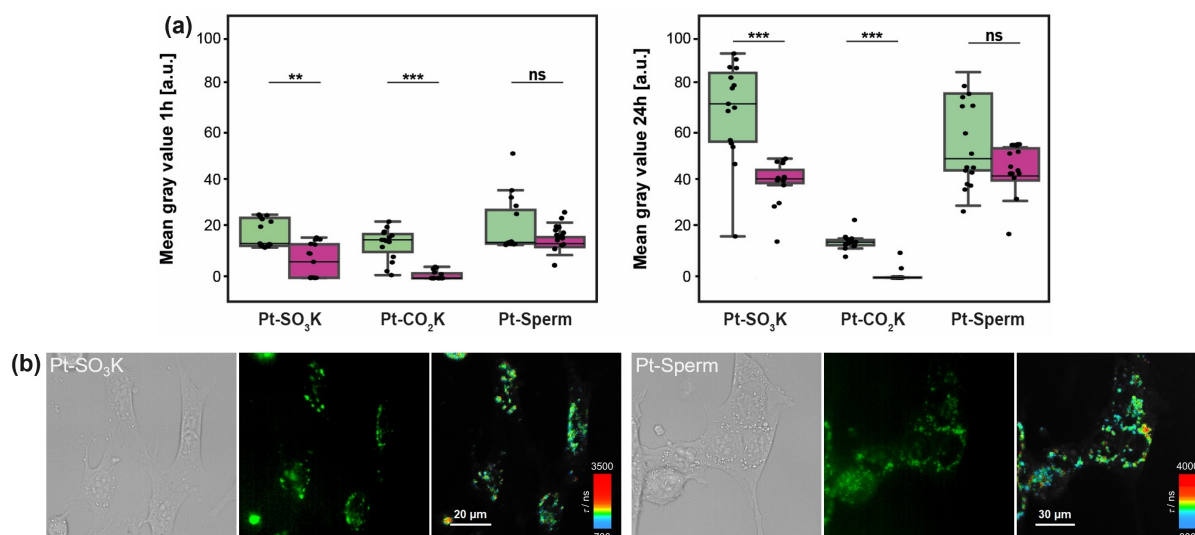
Chemistry–A European Journal

Research Article
doi.org/10.1002/chem.202404432

Chemistry
Europe
European Chemical
Societies Publishing

Figure 7. (a) Ratio quantification of the two channels (green 481-570 nm *vs.* red channel 590 - 680 nm) of **Pt-SO₃K**, **Pt-CO₂K** and **Pt-Sperm** on fibroblast cell lines after 1 h and 24 h of incubation. Box plots represent the median $\pm$ SD (n = 3). (b) Bright field, luminescence images and lifetime maps of living fibroblasts incubated with 10 μM **Pt-SO₃K** and **Pt-Sperm** in culture medium for 24 h at 37 °C (λ_{ex} = 375 nm; λ_{em} = 460 LP long-pass filter cutting off below 460 nm). ***P* < 0.01; ****P* < 0.001; ns, *P* ≥ 0.05.

environmental change and possible protection from physical quenchers, such as triplet dioxygen and H_2O. Since the aggregated nanostructures in solution had even shorter lifetimes due to ACQ (and the metal centers of such aggregates are already shielded from quenchers by metal-metal interactions and π-π-stacking), the formation of such structures can be confidently ruled out on the basis of the PLIM measurements at these concentrations, so that the emission in both channels can be assigned to the respective monomer.

To investigate the potential for interactions with cell organelles beyond lysosomes, the Pt(II)-complex localization was investigated in fixed cells after treatment with 4% paraformaldehyde (PFA) and Triton X100, followed by the incubation with **Pt-SO₃K**, **Pt-CO₂K** and **Pt-Sperm** (10 μM). Intriguingly, **Pt-Sperm** was specifically enriched in distinct structures in cell nuclei – presumably nucleoli (Figure 8). This

localization was not observed with **Pt-SO₃K**, **Pt-CO₂K** complexes (Figure S132) indicating a preferential binding that is mediated by the amphiphilic structure and the spermine chains, which are known to stabilize DNA.[24]

These results underline the different cellular distribution of the three complexes in living and fixed cells, due to their different structural features with a prominent ability observed for **Pt-Sperm** to interact with the nuclei in fixed cells.

Conclusions

In summary, we have designed, synthesized and characterized three amphiphilic Pt(II) complexes bearing tetradentate luminophores acting as bis-cyclometalated ligands that provide enhanced aqueous solubility. The self-assembly properties of
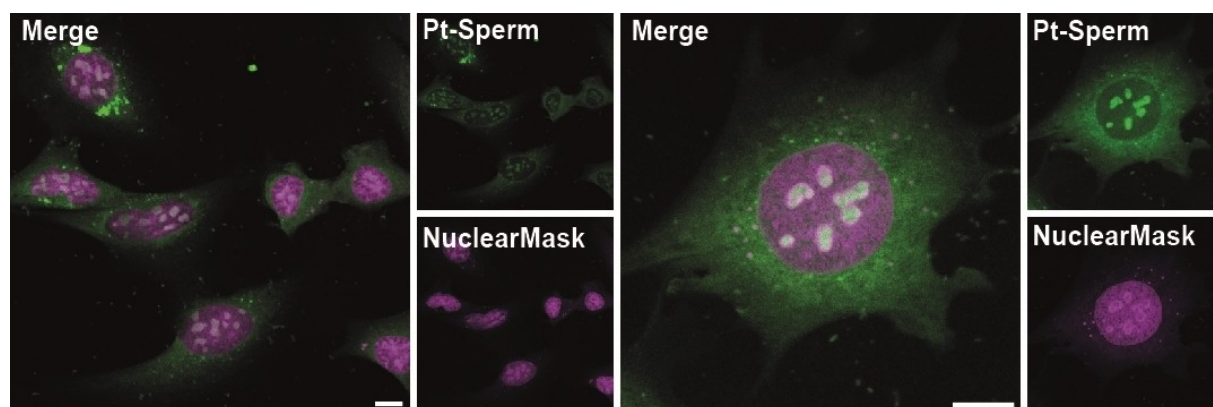

Figure 8. Confocal luminescence images (λ_{ex} = 405 nm; λ_{em} = 481 - 570 nm) and HCS NuclearMask™ stain (λ_{ex} = 633 nm; λ_{em} = 651 - 686 nm) of fixed and permeabilized fibroblast cells incubated with 10 μM **Pt-Sperm** in PBS for 24 h at room temperature. Overview image (left) and single cell image (right) show localization of **Pt-Sperm** within subnuclear structures (presumably in the nucleoli). Large images represent merged channels, small images show the individual emission channels. Scale bar 10 μm.

Chemistry–A European Journal

Research Article
doi.org/10.1002/chem.202404432

Chemistry
Europe
European Chemical
Societies Publishing

these compounds were investigated using a combination of photophysical characterization and morphological elucidation techniques, revealing their ability to form well-defined nanostructures. **Pt-SO₃K** and **Pt-CO₂K** exhibited a tunable photophysical behavior, including emission modulation influenced by concentration and solvent composition while self-assembling into micellar structures in aqueous environments. In contrast, **Pt-Sperm** remained predominantly monomeric with invariant photophysical properties within a broad range of variable conditions. Additionally, cellular studies revealed distinct uptake patterns, with **Pt-SO₃K**, **Pt-CO₂K** and **Pt-Sperm** localizing primarily in lysosomes of live fibroblast cells, underscoring their potential for bioimaging applications. PLIM images confirmed that these complexes remain monomeric within the cellular microenvironment, with lifetimes significantly longer than those observed in aqueous solutions, thus suggesting protection from physical quenching. In fixed cells, **Pt-Sperm** labelled subnuclear structures, reminiscent of nucleoli, indicating the potential for targeting these distinct organelles.

It is anticipated that the herein presented concepts provide further insights into the systematic design of supramolecular structures to manipulate Pt···Pt interactions. These are supported by balanced interactions between hydrophobic and hydrophilic units with responsiveness to variations in solvent environment and concentration. Due to their distinct interaction with different biological structures, they could be potentially used as biomarkers for specific organelles and subcellular compartments.

Author Contributions

Acknowledgements

Conflict of Interests

The authors declare no competing interests.

Data Availability Statement

The data supporting the findings of this study are provided in the supplementary information and are available from the corresponding author on request.

[1] a) E. Mattia, S. Otto, *Nat. Nanotechnol.* **2015**, *10*, 111; b) G. V. Oshovsky, D. N. Reinhoudt, W. Verboom, *Angew. Chem. Int. Ed.* **2007**, *46*, 2366; c) J.-M. Lehn, *Eur. Rev.* **2009**, *17*, 263.

[2] a) X. Zhang, C. Wang, *Chem. Soc. Rev.* **2011**, *40*, 94; b) C. Wang, Z. Wang, X. Zhang, *Acc. Chem. Res.* **2012**, *45*, 608.

[3] a) P. Xing, T. Sun, A. Hao, *RSC Adv.* **2013**, *3*, 24776; b) P. Zhang, X. Qian, Z. Zhang, C. Li, C. Xie, W. Wu, X. Jiang, *ACS Appl. Mater. Interfaces* **2017**, *9*, 5768; c) M. Ramanathan, L. K. Shrestha, T. Mori, Q. Ji, J. P. Hill, K. Ariga, *Phys. Chem. Chem. Phys.* **2013**, *15*, 10580; d) N. Feiner-Gracia, M. Buzhor, E. Fuentes, S. Pujals, R. J. Amir, L. Albertazzi, *J. Am. Chem. Soc.* **2017**, *139*, 16677.

[4] S. Zhang, R.-O. Moussodia, H.-J. Sun, P. Leowanawat, A. Muncan, C. D. Nusbaum, K. M. Chelling, P. A. Heiney, M. L. Klein, S. André, et al., *Angew. Chem. Int. Ed.* **2014**, *53*, 10899.

[5] a) J. Huang, X. Tan, C. Li, R. Wu, Y. Tao, T. Mou, *ACS Omega* **2022**, *7*, 18085; b) D. Wu, Y. Li, J. Yang, J. Shen, J. Zhou, Q. Hu, G. Yu, G. Tang, X. Chen, *ACS Appl. Mater. Interfaces* **2017**, *9*, 44392; c) C. M. A. Gangemi, R. Puglisi, A. Pappalardo, G. Trusso Sfrazzetto, *Bioorg. Med. Chem. Lett.* **2018**, *28*, 3290.

[6] V. W.-W. Yam, V. K.-M. Au, S. Y.-L. Leung, *Chem. Rev.* **2015**, *115*, 7589.

[7] T. Theiss, S. Buss, I. Maisuls, R. López-Arteaga, D. Brünink, J. Kösters, A. Hepp, N. L. Doltsinis, E. A. Weiss, C. A. Strassert, *J. Am. Chem. Soc.* **2023**, *145* (7), 3937–3951.

[8] C. Po, A. Y.-Y. Tam, K. M.-C. Wong, V. W.-W. Yam, *J. Am. Chem. Soc.* **2011**, *133*, 12136.

[9] M. Mauro, A. Aliprandi, C. Cebrián, Di Wang, C. Kübel, L. de Cola, *Chem. Commun.* **2014**, *50*, 7269.

[10] J. Li, K. Chen, J. Wei, Y. Ma, R. Zhou, S. Liu, Q. Zhao, W.-Y. Wong, *J. Am. Chem. Soc.* **2021**, *143*, 18317.

[11] a) S. C. F. Kui, I. H. T. Sham, C. C. C. Cheung, C.-W. Ma, B. Yan, N. Zhu, C.-M. Che, W.-F. Fu, *Chem. Eur. J.* **2007**, *13*, 417.

[12] Z. Chen, A. K.-W. Chan, V. C.-H. Wong, V. W.-W. Yam, *J. Am. Chem. Soc.* **2019**, *141*, 11204.

[13] W. Zhang, W. Jin, T. Fukushima, N. Ishii, T. Aida, *Angew. Chem. Int. Ed.* **2009**, *48*, 4747.

[14] M. E. Robinson, A. Nazemi, D. J. Lunn, D. W. Hayward, C. E. Boott, M.-S. Hsiao, R. L. Harniman, S. A. Davis, G. R. Whittell, R. M. Richardson, et al., *ACS Nano.* **2017**, *11*, 9162.

[15] B. Yang, H. Ni, H. Wang, Y. Hu, K. Luo, W. Yu, *J. Phys. Chem. C* **2020**, *124*, 23879.

[16] M. E. Gutierrez Suburu, M. Blanke, L. Geerkens, A. Hepp, I. Maisuls, J. Kösters, T. Neumann, J. Voskuhl, M. Giese, C. A. Strassert, *Aggregate* **2024**, *5*.

[17] a) Y. Li, L. Chen, Y. Ai, E. Y.-H. Hong, A. K.-W. Chan, V. W.-W. Yam, *J. Am. Chem. Soc.* **2017**, *139*, 13858; b) Y. Atoini, E. A. Prasetyanto, P. Chen, S. Silvestrini, J. Harrowfield, L. de Cola, *Chem. Eur. J.* **2018**, *24*, 12054; c) I. Maisuls, C. Wang, M. E. Gutierrez Suburu, S. Wilde, C.-G. Daniliuc, D. Brünink, N. L. Doltsinis, S. Ostendorp, G. Wilde, J. Kösters et al., *Chem. Sci.* **2021**, *12*, 3270.

[18] X. Zhen, R. Qu, W. Chen, W. Wu, X. Jiang, *Biomater. Sci.* **2021**, *9*, 285.

[19] M. E. Gutierrez Suburu, I. Maisuls, J. Kösters, C. A. Strassert, *Dalton Trans.* **2022**, *51*, 13342.

[20] A. V. Davis, R. M. Yeh, K. N. Raymond, *Proc. Natl. Acad. Sci. USA* **2002**, *99*, 4793.

Chemistry–A European Journal

Research Article
doi.org/10.1002/chem.202404432

Chemistry Europe
European Chemical
Societies Publishing

[21] a) K. Hasan, A. K. Bansal, I. D. W. Samuel, C. Roldán-Carmona, H. J. Bolink, E. Zysman-Colman, *Sci. Rep.* **2015**, *5*, 12325; b) J. Brooks, Y. Babayan, S. Lamansky, P. I. Djurovich, I. Tsyba, R. Bau, M. E. Thompson, *Inorg. Chem.* **2002**, *41*, 3055.

[22] a) B. Del Rio, B. Redruello, D. M. Linares, V. Ladero, P. Ruas-Madiedo, M. Fernandez, M. C. Martin, M. A. Alvarez, *Food Chem.* **2018**, *269*, 321; b) S. Sharmin, K. Sakata, K. Kashiwagi, S. Ueda, S. Iwasaki, A. Shirahata, K. Igarashi, *Biochem. Biophys. Res. Com.* **2001**, *282*, 228; c) J.-G. Delcros, S. Tomasi, S. Carrington, B. Martin, J. Renault, I. S. Blagbrough, P. Uriac, *J. Med. Chem.* **2002**, *45*, 5098–5111.

[23] A. M. Mansour, K. Radacki, O. R. Shehab, *Dalton Trans.* **2021**, *50*, 10701.

[24] a) B. G. Feuerstein, N. Pattabiraman, L. J. Marton, *Nucleic Acids Res.* **1990**, *18*, 1271; b) N. Seiler, J. G. Delcros, J. P. Moulinoux, *Int. J. Biochem. Cell. Biol.* **1996**, *28*, 843.

[25] a) G. R. Fulmer, A. J. M. Miller, N. H. Sherden, H. E. Gottlieb, A. Nudelman, B. M. Stoltz, J. E. Bercaw, K. I. Goldberg, *Organometallics* **2010**, *29*, 2176; b) A. J. Geall, I. S. Blagbrough, *Tetrahedron* **2000**, *56*, 2449; c) T. Rex, S. Baumert, A. Hepp, G. Fernandez, C. A. Strassert, *Chem. Sci.* **2024**, *15*, 18881.